Vietnam Journal of Catalysis and Adsorption
Tạp chí xúc tác và hấp phụ Việt Nam

https://jca.edu.vn

Oxidation-Level-Tailored rGO in Fe_3O_4/CuO/rGO Nanocomposites: Comprehensive Structural and Thermal Characterization for Enhanced Ammonium Perchlorate Decomposition

Vu Tien Cong[1,2,*], Vu Minh Thanh[1], Nguyen Duc Long[2]

[1] *Institution of Chemistry, Biology and Environment – Academy of Militaty Science and Technology, 17 Hoang Sam street, Hanoi, VIETNAM*
[2] *Institution of Propellants and Explosives – Vietnam Defence Industry, 192 Duc Giang street, Hanoi, VIETNAM*
** Email: congph40@gmail.com*

ARTICLE INFO

Received: 06/08/2025
Accepted: 11/09/2025
Published: 30/09/2025

Keywords:
rGO Oxidation level;
Fe_3O_4/CuO/rGO nanocomposite;
ammonium perchlorate decomposition;
composite propellant

ABSTRACT

A Fe_3O_4/CuO/rGO nanocomposite was synthesized via an ultrasonic-assisted co-precipitation method. Reduced graphene oxide (rGO) with varying oxidation levels was prepared by controlled thermal reduction of graphene oxide in air and subsequently incorporated into the nanocomposite. The structural, morphological, and textural properties were characterized using X-ray diffraction (XRD), Raman spectroscopy, scanning electron microscopy with energy-dispersive X-ray spectroscopy (SEM-EDX), and nitrogen adsorption–desorption analysis (BET). The catalytic performance toward the thermal decomposition of ammonium perchlorate (AP) was evaluated by thermogravimetric analysis (TGA). Uniformly dispersed Fe_3O_4/CuO nanoparticles with diameters of 8–20 nm were observed on the rGO sheets. The nanocomposite containing rGO annealed at 250 °C for 4.5 hours exhibited a high specific surface area of 187.2 m^2/g and significantly reduced the AP decomposition temperature by 112.4 °C, highlighting the critical influence of rGO oxidation level on the catalytic performance of the Fe_3O_4/CuO/rGO system.

Introduction

In composite propellants, ammonium perchlorate (AP) remains the dominant oxidizer (50–80 wt%), so the combustion behavior of AP has a direct impact on the burning rate of propellants which is a parameter that consistently needs to be enhanced. [1]. Pure AP decomposes in two high-temperature stages (high-temperature decomposition, HTD, ~380–450 °C) with limited exothermicity. Catalysts lower the decomposition temperature and increase heat release, thereby enhancing burning rates [2]. Transition-metal oxides (e.g., Fe_2O_3, CuO, NiO, Co_3O_4) are effective-particularly as nanoparticles—although agglomeration impedes dispersion and activity[3-5]. Graphene-based supports (graphene, graphene oxide, GO, and reduced graphene oxide, rGO) mitigate this limitation: GO provides oxygenated functional groups that promote nanoparticle anchoring and dispersibility, whereas rGO offers superior thermal conductivity conducive to stable combustion surfaces [5]. Representative catalyst systems, such as Fe_2O_3/GO (ΔT_{HTD} ≈ −77 °C) [5], CuO/graphene (ΔT_{HTD} ≈ −107 °C)[4], GO:CuO = 1:2 (ΔT_{HTD} ≈ −99 °C)[6], and $CoFe_2O_4$/rGO (ΔT_{HTD} ≈ −57.4 °C) [7], consistently depress AP's HTD and often increase burning rates. These results demonstrate that

https://doi.org/10.62239/jca.2025.042
82

GO and rGO are promising substrates for new catalysts for the decomposition of AP.

rGO can be obtained from GO via thermal, chemical, or radiation-induced reduction [8-10]. Among these, Thermal reduction is operationally simple and cost-effective; although it does not yield pristine graphene, the defects introduced provide anchoring sites for metal-oxide nanoparticles, which is advantageous for AP-decomposition catalysts. Although rGO has been extensively investigated, the influence of oxidation level—defined by defect density and oxygen-functional-group content—on metal-oxide/graphene nanocomposites remains insufficiently resolved. In our previous work, Fe_3O_4/CuO/graphene exhibited strong activity, yet nanoparticles preferentially localized at defect-rich sheet edges bearing residual oxygen functionalities [11]. In this work, Fe_3O_4/CuO/rGO nanocomposites were synthesized using rGO produced by thermal reduction of GO under varied air-annealing conditions, enabling a systematic evaluation of how rGO oxidation level affects catalytic performance in AP decomposition.

Experimental

Chemical

The study employed high-purity analytical-grade chemicals sourced from Merck, including Iron(II) chloride tetrahydrate ($FeCl_2.4H_2O$, ≥99.9%), Iron(III) chloride hexahydrate ($FeCl_3.6H_2O$, ≥99.9%), Copper(II) chloride dihydrate ($CuCl_2.2H_2O$, ≥99.9%), Sodium hydroxide (NaOH, ≥99.5%), and Hydroxylamine hydrochloride ($NH_2OH.HCl$, ≥98.0%). Graphene oxide (GO), nitrogen gas (N_2, ≥99.9%), and ethanol (≥99.5%) were obtained from domestic suppliers in Vietnam..

Methods

Thermal reducing of GO

To obtain reduced graphene oxides (rGO) with different oxidation levels, graphene oxide (GO) was evenly spread over the bottom surface of a glass beaker. The rGO-200-1.5 and rGO-200-4 samples were heated from 30 to 200 °C over 1 h and then held at 200 °C for 1.5 h and 4 h, respectively. The rGO-250-4.5 sample was heated from 30 to 130 °C over 20 min (held 20 min), then from 130 to 250 °C over 20 min, and finally held at 250 °C for 4.5 h.

Synthesis of CuO/Fe_3O_4/GO (or rGO) nanocomposites

The following precursor solutions were prepared in advance: 0.5 M $FeCl_3$, 0.5 M $CuCl_2$, 0.25 M $FeCl_2$, 1 M NaOH, and 0.1 M $NH_2OH.HCl$. Notably, the 0.25 M $FeCl_2$ solution was freshly prepared on the day of synthesis. An amount of 0.1 g GO (or thermally reduced rGO) was weighed into a beaker. Then, 3.5 mL of the $FeCl_2$ and $FeCl_3$ solutions were added to the beaker, which was placed in a thermostatic water bath at the designated temperature. A pH probe and an ultrasonic probe were immersed into the reaction mixture, while nitrogen gas was continuously bubbled over the surface at a flow rate of approximately 2 mL/min throughout the synthesis. NaOH solution was added dropwise until the pH reached 12. Two minutes after reaching this pH, 5 mL of $CuCl_2$ solution was added. NaOH addition continued until the pH again stabilized at 12. Ultrasonication was maintained until a total sonication time of 45 minutes was reached.

After completion, the reaction mixture was left undisturbed for 12 hours. The supernatant was decanted, and the residue was collected by centrifugation. The residue was washed and centrifuged 3–4 times using deionized water. During each wash, 1–2 drops of $NH_2OH.HCl$ solution were added to maintain pH stability. Washing was continued until the pH of the wash water reached neutrality (confirmed using pH indicator paper). Finally, the product was washed with ethanol, centrifuged, and then dried at 60 °C for 12 hours.

Material characterizations

X-ray diffraction (XRD) patterns were collected on a D8 Advance diffractometer (Bruker) using monochromatic Cu Kα radiation (λ = 1.5406 Å) at 40 kV and 40 mA over 2θ = 5–70° with a 0.0297° step. Raman spectra were acquired on a DXR3 spectrometer (Thermo Scientific) with 532 nm excitation; the inter-defect distance LDL_DLD was calculated using Equation (3) of Cançado et al. [12]. Textural properties were measured by N_2 sorption - BET (Tristar II 3030 Plus, G&G Instrument). Surface morphology and elemental distributions were examined by SEM and SEM–EDX mapping (Hitachi S-4800).

For catalytic testing toward ammonium perchlorate (AP) decomposition, AP was blended with 5 wt% catalyst by grinding in an agate mortar. Thermal behavior was evaluated by TGA (Labsys TGA 1600) under N_2 at 10 °C min^{-1} from room temperature to 900 °C (~15 mg samples). Data processing and plotting used OriginPro 2024. Raman D and G bands were fitted with Lorentzian profiles following [13].

Results and discussion

Properties of thermally reduced rGO

https://doi.org/10.62239/jca.2025.042

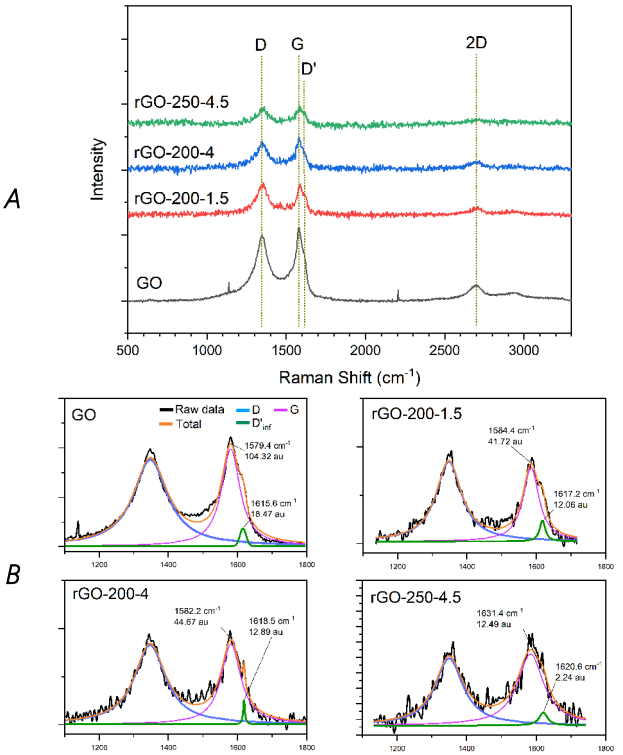

Fig 1: Raman spectra of GO and rGO samples thermally treated under different conditions (A) and Deconvolution of Band D and G for determination of peak G and D' (B)

Raman spectroscopy provides valuable insights into the defect characteristics of GO and the rGO samples obtained after thermal reduction (Fig 1A). All acquired spectra exhibit characteristic peaks of graphitic materials: the D band (~1340 cm^{-1}), G band (~1580 cm^{-1}), D' band (~1620 cm^{-1}), and 2D band (~2700 cm^{-1}). The D band is associated with structural defects and edge sites, while the G band corresponds to the in-plane vibration of sp^2 carbon atoms. The ratio of ID/IG (D and G peak intensities) reflects the density of structural defects. As summarized in Table 1, the initial thermal treatment at 200 °C for 1.5 h caused a significant increase in the ID/IG ratio, indicating a rapid deoxygenation process that introduced lattice vacancies. However, prolonged or more intense thermal treatment resulted in a decrease in this ratio, suggesting partial reorganization of the sp^2 domains and an increase in the average inter-defect distance (L_D). The 2D band, which provides information about the graphitic stacking order, became broader and progressively weaker—nearly merging with the baseline—as temperature and duration increased. Interestingly, the I_2D/IG ratio remained relatively unchanged between GO and rGO-200-1.5, but showed a notable increase in the rGO-250-4.5 sample. This suggests a tendency for restacking of graphene layers after removal of interlayer oxygen-containing groups, which is consistent with observations from the D band behavior.

The D' band, indicative of defects introduced by oxygen-containing surface functional groups, appears as a shoulder adjacent to the G band. King et al. [13] proposed the use of the ID'_{inf}-IG index (where ID'_{inf} > is the interpolated intensity of the D' band extracted from the deconvolution of the G band (Fig 1B)—as a more systematic indicator of the oxygen-functional group content in GO materials. As shown in Table 1, all samples exhibit ID'_{inf}-IG values lower than 0, which, according to the classification by King et al. [13] , indicates that these materials cannot yet be classified as reduced graphene oxide (rGO), which requires 0< ID'_{inf}-IG <25. Nonetheless, thermal treatment clearly increases this index from –85.85 to –10.25, signifying a notable decrease in oxygen functional groups and, consequently, an increase in the C/O ratio with higher temperature and longer heating durations.

Table 1: Summary of calculated defect-related parameters for GO and rGO samples.

Sample	ID/IG	I_2D/IG	L_D(nm)	ID'_{inf}-IG
GO	0.91	0.23	12.6	-85.85
rGO-200-1.5h	1.06	0.24	11.7	-29.66
rGO-200-4h	0.94	0.21	12.4	-31.78
rGO-250-4.5h	0.97	0.28	12.2	-10.25

Properties of the Nanocomposite Materials

XRD analysis

The X-ray diffraction (XRD) patterns of the nanocomposite samples prepared on GO and various rGO substrates (Fig 2) revealed distinct diffraction peaks corresponding to the CuO phase (Tenorite, PDF 00-048-1548), with characteristic peaks at 2θ ≈ 38.7°, 35.5°, 48.7°, and 32.5°, attributed to the (111), (–111), (–202), and (110) crystal planes, respectively [14]. These CuO peaks were observed in all four samples. In addition, the Fe_3O_4 phase (Magnetite, PDF 01-071-6336), showing characteristic peaks at 2θ ≈ 35.5°, 62.7°, 30.2°, and 58.5°—corresponding to the (311), (440), (220), and (511) planes—was clearly visible in the samples based on GO and rGO-200-1.5h but absent in the other two. This may be due to strong interactions between the rGO substrate and Fe–OH species, where drying at 60 °C was insufficient to complete the Fe_3O_4 crystallization. Furthermore, the possible formation of extremely small or amorphous Fe–O–C structures may have contributed to signal broadening or

https://doi.org/10.62239/jca.2025.042

disappearance in the XRD patterns, which is consistent with observations from SEM and SEM–EDX images.

Regarding the GO phase, the characteristic diffraction peak at 2θ ≈ 10° (001), which corresponds to oxygen-containing functional groups intercalated between GO layers, was absent in all four samples. This confirms that ultrasonication effectively exfoliated the GO and rGO layers. Moreover, the (002) peak at 2θ ≈ 26.5°, which appeared sharp and intense in the GO-based sample, became weaker and broader in the rGO-based samples. This indicates a gradual loss in crystallinity, consistent with partial delamination of rGO layers in the nanocomposites. The appearance of the (002) peak along with the disappearance of the (001) peak also suggests that the GO substrate underwent partial reduction during synthesis [15], implying the formation of direct bonds between the oxides and the GO/rGO support.

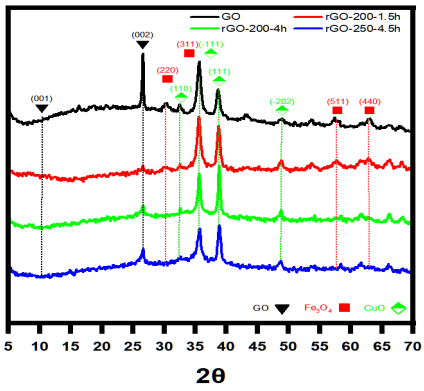

Fig 2: XRD patterns of nanocomposite samples synthesized on GO and thermally reduced rGO substrates.

SEM and SEM-EDX mapping analysis

SEM (Fig. 3) shows well-dispersed CuO crystals - rhomboid, monoclinic [14] , ~100–200 nm long and ~8–20 nm wide - together with Fe_3O_4 particles (cubic/FCC lattice) [16]. Particles are intercalated between GO layers and partly decorate sheet surfaces, with number density increasing as thermal reduction intensifies. In rGO-250-4.5 (Fig. 3D), the oxides appear as fine dots across rGO basal planes, indicating bonding at both edges and defect sites. This implies that air-annealing generates vacancies that act as nucleation centers. Correspondingly, CuO crystals in this sample are sharper and thinner, consistent with enhanced, multidirectional nucleation and growth; similar considerations likely govern Fe_3O_4 formation.

Elemental mapping (Fig. 4E) of rGO-250-4.5 confirms Fe, Cu, and O uniformly distributed over the Carbon matrix. Although Fe_3O_4 is not resolved by XRD, the Fe signal suggests an amorphous phase or strong interfacial bonding to rGO. The near-identical Fe/Cu maps indicate homogeneous composite formation, while widespread dark regions point to a highly porous morphology.

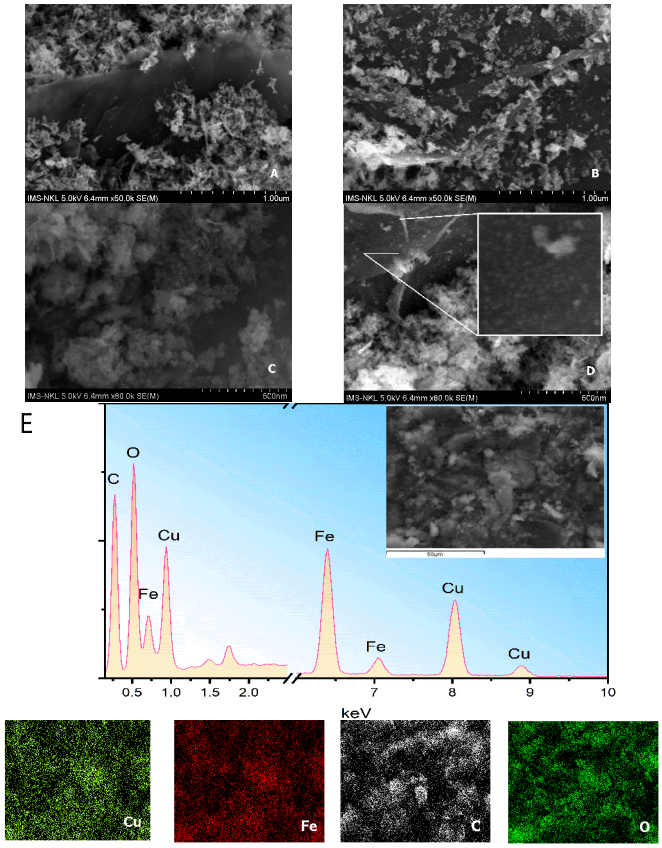

Fig 3: SEM images of nanocomposites synthesized on GO (A), rGO-200-1.5 (B), rGO-200-4 (C), and rGO-250-4.5 (D) substrates; *with the* EDX elemental mapping of the nanocomposite sample based on rGO-250-4.5 (E)

BET analysis

The nitrogen adsorption–desorption isotherms (Fig 4) exhibit typical type IV(a) behavior with H2(b)-type hysteresis loops [17], indicating that the nanocomposites possess mesoporous structures, likely tube- or cone-shaped, with pore sizes mainly in the range of 5–10 nm. The presence of pore blocking due to narrow pore necks, commonly observed in thermally treated materials, was evident. Notably, the higher temperature treatment at 250 °C helped reduce the extent of pore blocking, resulting in a narrower hysteresis loop compared to those treated at 200 °C. This is also agreement with the superior surface area and pore volume of the rGO-250-4.5-based nanocomposite (187.2 m^2/g and 0.845 cc/g, respectively) compared to rGO-200-1.5 (151.59 m^2/g, 0.803 cc/g) and rGO-200-4 (137.68 m^2/g, 0.630 cc/g). These characteristics suggest that the rGO-250-4.5 sample may offer enhanced catalytic performance for AP decomposition.

https://doi.org/10.62239/jca.2025.042

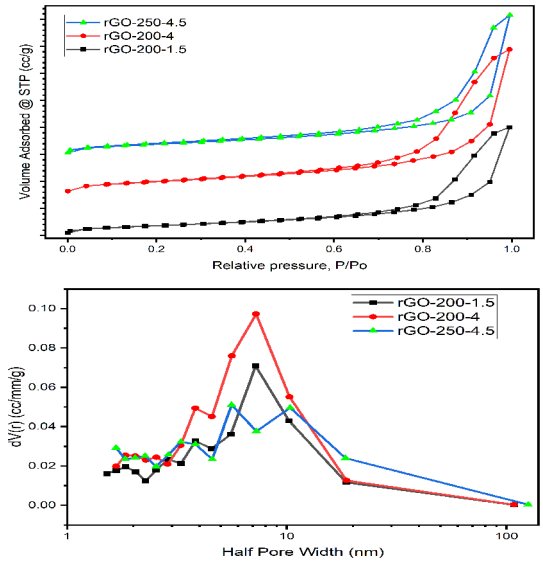

Fig 4: BET isotherms and pore size distribution of nanocomposites based on different rGO substrates

Catalytic Performance Toward AP Decomposition

The catalytic activity of Fe_3O_4/CuO/rGO nanocomposites was evaluated by mixing 5 wt% of each sample with AP, followed by thermogravimetric analysis (TGA). For comparison, pure AP and a previously studied nanocomposite based on graphene (G-Comp) were also analyzed [11] (Fig 5). The results demonstrated that all nanocomposites significantly enhanced the thermal decomposition of AP. This was evidenced by steeper TGA curves during the decomposition phase, narrower dTG peaks, and near-complete decomposition below 450 °C, with residual mass below 2%, suggesting that the catalyst was fully consumed or carried off during combustion. Importantly, the AP decomposition temperature was substantially reduced by the nanocomposites. The observed reductions were 102 °C, 106.8 °C, 109 °C, and 112.4 °C for GO-Comp, rGO-200-1.5-Comp, rGO-200-4-Comp, and rGO-250-4.5-Comp, respectively. These results align with the BET findings and indicate that improved porosity and surface area contribute to enhanced catalytic effects. In comparision with G-Comp (graphene-based catalyst), the catalytic performance of the GO-based nanocomposite (with the highest oxidation level) led to an additional 11.3 °C reduction in decomposition temperature. This enhancement increased progressively to a 21.7 °C reduction for the rGO-250-4.5-based nanocomposite, which exhibited lower oxidation levels and restacking behavior. These findings suggest that the oxidation degree of rGO plays a more crucial role in AP decomposition catalysis than merely its electronic or thermal conductivity.

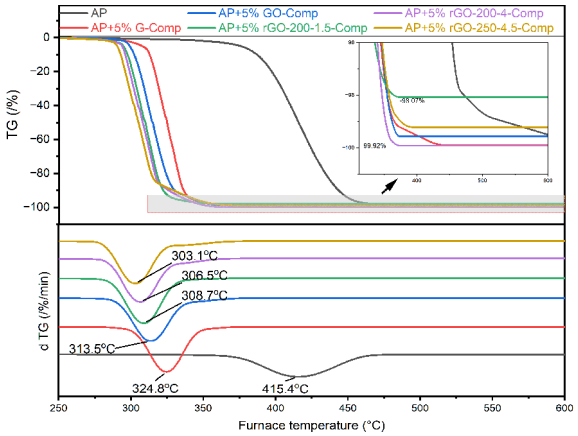

Fig 5: Comparison of AP decomposition promoted by Fe_3O_4/CuO nanocomposites based on GO, rGO, and graphene (adapted from previous research [11])

Conclusion

A series of Fe_3O_4/CuO/rGO nanocomposites were successfully synthesized using rGO obtained by thermal reduction of GO under various air-based heating conditions. The study reveals that the oxidation degree of rGO—including both the abundance of oxygen-containing functional groups and the density of structural defects—has a significant impact on its catalytic performance toward AP decomposition. The nanocomposites were synthesized via a simple co-precipitation method without requiring post-synthesis calcination. The oxidation level of rGO was shown to affect the crystallization of oxide phases and promote favorable interactions that enable uniform dispersion of metal oxides across the rGO sheets, thus enhancing catalytic effectiveness. Among the tested samples, the nanocomposite based on rGO-250-4.5 (thermally treated at 250 °C for 4.5 h) exhibited the highest BET surface area (187.2 m^2/g), expanded mesopores, and evidence of rGO layer restacking. These properties contributed to the strongest catalytic effect, reducing the AP decomposition temperature by up to 112.4 °C. This highlights the material's strong potential as a combustion catalyst for composite solid propellants containing AP.

Acknowledgments

This research is funded by Institution of Propellants and Explosives and Institution of Chemistry, Biology and Environment. The authors declare no competing financial interest.

References

1. S. Li, Y. Song, C. Zhang, C. Zhao, J. Liu, R. Yang, Y. Tian, Y. Tang, RSC Adv. 12 (35) (2022) 22806–22814. https://doi.org/10.1039/D2RA03772F
2. A. Dey, J. Athar, P. Varma, H. Prasant, A.K. Sikder, S. Chattopadhyay, RSC Adv. 5 (3) (2015) 1950–1960. https://doi.org/10.1039/C4RA10812D
3. Z. Shi, C. Huang, H. Li, J. Zhang, Y. Han, Z. Li, ChemNanoMat 8 (6) (2022) e202200118. https://doi.org/10.1002/cnma.202200118
4. M.A. Fertassi, H. Bensaid, S. Chahboun, A. El Hamidi, A. Mokhlisse, RSC Adv. 6 (78) (2016) 74155–74161. https://doi.org/10.1039/C6RA13261H
5. J. Pei, H. Zhao, F. Yang, D. Yan, Langmuir 37 (20) (2021) 6132–6138. https://doi.org/10.1021/acs.langmuir.1c00108
6. D. Li, X. Li, X. Xu, H. Zhao, L. Wang, X. Sun, X. Xu, ACS Omega 8 (25) (2023) 22876–22886. https://doi.org/10.1021/acsomega.3c01865
7. X. Hou, M. Zhang, F. Zhao, H. Li, Y. Zuo, R. Li, in: International Conference on Development and Application of Carbon Nanomaterials in Energetic Materials, Springer, 2021, pp. 227–234.
8. I. Sengupta, S. Chakraborty, M. Talukdar, S.K. Pal, S. Chakraborty, J. Mater. Res. 33 (23) (2018) 4113–4122. https://doi.org/10.1557/jmr.2018.338
9. N.G. de Barros, R. Fiorot, L. Parreira, E.S. Gonçalves, C 9 (3) (2023) 73. https://doi.org/10.3390/c9030073
10. C.-M. Chen, Q. Zhang, M.-G. Yang, C.-H. Huang, Y.-G. Yang, M.-Z. Wang, Carbon 50 (10) (2012) 3572–3584. https://doi.org/10.1016/j.carbon.2012.03.029
11. V.T. Cong, N.D. Long, N.T. Huong, V.M. Thanh, ACS Omega 10 (31) (2025) 34331–34341. https://doi.org/10.1021/acsomega.5c01750
12. L.G. Cançado, A. Jorio, E.H.M. Ferreira, F. Stavale, C.A. Achete, R.B. Capaz, M.V.O. Moutinho, A. Lombardo, T.S. Kulmala, A.C. Ferrari, Nano Lett. 11 (8) (2011) 3190–3196. https://doi.org/10.1021/nl201432g
13. A.A. King, J.D. Babrah, L. Gannon, J.A. Robinson, D.A. Muller, P.J. Withers, R.J. Young, Sci. Rep. 6 (2016) 19491. https://doi.org/10.1038/srep19491
14. S. Åsbrink, L.-J. Norrby, Acta Crystallogr. Sect. B Struct. Crystallogr. Cryst. Chem. 26 (1) (1970) 8–15. https://doi.org/10.1107/S0567740870001838
15. S.A. Soomro, I.H. Gul, H. Naseer, S. Marwat, M. Mujahid, Curr. Nanosci. 15 (4) (2019) 420–429. https://doi.org/10.2174/1573413714666181115122016
16. W. Bragg, Nature 95 (2386) (1915) 561. https://doi.org/10.1038/095561a0
17. M. Thommes, K. Kaneko, A.V. Neimark, J.P. Olivier, F. Rodriguez-Reinoso, J. Rouquerol, K.S.W. Sing, Pure Appl. Chem. 87 (9–10) (2015) 1051–1069. https://doi.org/10.1515/pac-2014-1117